

## Use of Synthetic Aperture Radar in Finescale Surface Analysis of Synoptic-Scale Fronts at Sea

G. S. YOUNG

*Department of Meteorology, The Pennsylvania State University, University Park, Pennsylvania*

T. D. SIKORA

*Department of Oceanography, United States Naval Academy, Annapolis, Maryland*

N. S. WINSTEAD

*Applied Physics Laboratory, The Johns Hopkins University, Baltimore, Maryland*

(Manuscript received 8 March 2004, in final form 6 December 2004)

### ABSTRACT

The viability of synthetic aperture radar (SAR) as a tool for finescale marine meteorological surface analyses of synoptic-scale fronts is demonstrated. In particular, it is shown that SAR can reveal the presence of, and the mesoscale and microscale substructures associated with, synoptic-scale cold fronts, warm fronts, occluded fronts, and secluded fronts. The basis for these findings is the analysis of some 6000 *RADARSAT-1* SAR images from the Gulf of Alaska and from off the east coast of North America. This analysis yielded 158 cases of well-defined frontal signatures: 22 warm fronts, 37 cold fronts, 3 stationary fronts, 32 occluded fronts, and 64 secluded fronts. The potential synergies between SAR and a range of other data sources are discussed for representative fronts of each type.

### 1. Introduction

Finescale surface analysis of synoptic-scale weather systems is a challenging undertaking in the best of circumstances, but has proven particularly difficult at sea because of the paucity of in situ observations (Young et al. 1997; Bosart 2003). Remote sensing has taken a lead role in mitigating this problem. The success of remote sensing in this respect depends on the nature of the phenomena being analyzed, the quantity being measured by the remote sensor, and the ratio of the scales of interest to the spatial resolution of the remote sensor. For example, lower-tropospheric streamline analysis via visible or infrared cloud track winds would be problematic under cirrus overcast while a microwave scatterometer would face no such difficulty. Table 1 summarizes the operationally salient features of both in situ and remotely sensed surface observations (refer to Table 2 for definitions of meteorological scales found within Table 1). The key insight from the summary of sensor characteristics found in Table 1 is that no one

sensor can meet all of the analyst's needs. It is only by using the available sensors synergistically that a finescale marine surface analysis may be prepared. Note C-MAN in Table 1 refers to Coastal-Marine Automated Network.

Taken together, the diverse capabilities of these traditional observational data sources at best allow the marine analyst to locate and detail synoptic-scale fronts with a resolution up to the meso- $\beta$  scale. This is not, however, an all-weather high-resolution capability. Thus, a need remains to supplement the above-mentioned data sources with an all-weather high-resolution remote sensor for detecting synoptic-scale fronts at sea. Spaceborne synthetic aperture radar (SAR) provides just such a capability.

SAR offers particularly intriguing opportunities for improving the accuracy and resolution of marine surface analyses because of its ability to sense the ocean surface footprints of atmospheric processes, regardless of daylight and cloud conditions, and its order 10–100-m spatial resolution (e.g., Beal et al. 1981; Mourad 1999; Sikora et al. 2005). Thus, SAR opens the possibility of conducting finescale surface analyses of marine weather systems, as Friedman et al. (2001) demonstrated using several polar mesoscale cyclone case studies.

---

*Corresponding author address:* George Young, Dept. of Meteorology, The Pennsylvania State University, 503 Walker Bldg., University Park, PA 16802-5013.  
E-mail: young@ems.psu.edu

TABLE 1. Traditional data sources for marine surface analysis and their relevant characteristics.

Sensor	Platform	Measurements	Resolution	Frequency
In situ	Moored and drifting buoys, C-MAN coastal stations, ships	Vector wind, air temperature, sea temperature, humidity	Meso- $\beta$ -scale spacing where available	Hourly
Microwave scatterometer	Polar-orbiting satellite	Vector wind	Meso- $\beta$ scale (12.5-km pixels)	2–4 times daily
IR imagery	Polar-orbiting and geostationary satellites	Cloud-top temperature	Meso- $\gamma$ scale (1–4-km pixels)	4–48 times daily
Visible imagery	Polar-orbiting and geostationary satellites	Cloud patterns	Meso- $\gamma$ scale (1-km pixels)	4–48 times daily
Cloud-track winds	Geostationary satellites	Boundary layer vector wind	Meso- $\beta$ scale where appropriate clouds are present	Up to 48 times daily

### a. Basics of synthetic aperture radar

Typical SAR wavelengths are on the order of centimeters to decimeters. It follows then that there is little attenuation of the radar signal by the intervening atmosphere. Once the SAR's radiation reaches the ocean surface, the electromagnetic properties of which are quite homogeneous, penetration is limited to about a tenth of the wavelength of the radar. Thus, SAR backscatter from the ocean results from sea surface roughness elements having a wavelength on the order of that of the radar. That sea surface roughness is a result of the centimeter-scale wind-induced wave state. In general, the stronger the current-relative near-surface wind speed, the higher the SAR backscatter, and the brighter a SAR pixel. Current-relative wind direction also affects the SAR backscatter. At moderate incident angles, a major maximum occurs when the current-relative wind is blowing opposite the look direction of the radar and a minor maximum occurs when the current-relative wind is blowing in the same direction as the look direction of the radar. Minima occur when the current-relative wind blows perpendicular to the radar look direction.

Patterns in SAR backscatter from the ocean result from corresponding modulations of the centimeter-scale wind-induced wave state by both oceanic and atmospheric phenomena. Given the aforementioned high resolution of typical SARs, and their order 100–1000-km swath widths, they are ideal instruments for sensing

the sea surface signatures of those phenomena over a wide range of scales. Examples of signatures of oceanic phenomena imaged by SAR include swell, internal waves, surface currents, and sea surface slicks (see Jackson and Apel 2004). Sikora et al. (2005) provide a review of the signatures of atmospheric phenomena commonly imaged by SAR, including convective cells, roll vortices, gravity waves, mesoscale cyclones, and synoptic-scale weather systems. We note that in the near future related experimental products such as SAR-derived wind speed datasets (e.g., Horstmann et al. 2003; Monaldo et al. 2004) will have the potential of furthering the field of SAR meteorology.

### b. Scope

In this paper, we will demonstrate the viability of SAR as a tool for finescale marine meteorological surface analyses of synoptic-scale fronts using data from the Canadian Space Agency's *RADARSAT-1*. In doing so, we will show how SAR can reveal the presence of synoptic-scale cold fronts, warm fronts, occluded fronts, and secluded fronts, and their mesoscale and microscale substructures. Moreover, we will use some of the examples to highlight the synergy that can be obtained between SAR and traditional observational data sources.

Our study regions are the Gulf of Alaska and the northwestern Atlantic Ocean. These study regions were determined by the availability of a large number of *RADARSAT-1* SAR images from the Alaska SAR Demonstration (Monaldo 2000). These SAR data were processed by the Alaska SAR facility. Of the 6000 Alaska SAR Demonstration images available for examination (spanning the time period 15 December 1998–15 August 2003), approximately 90% were from the Gulf of Alaska and the Bering Sea with the remainder from the east coast of North America between the east coast of Florida and New England.

The SAR on board *RADARSAT-1* is C band (5.6 cm) and right looking with horizontal–horizontal polarization (HH-pol). The *RADARSAT-1* SAR has various sensor modes but the one employed here is the

TABLE 2. The Orlanski (1975) meteorological-scale definitions. The macro- $\alpha$  is also called the planetary scale and macro- $\beta$  the synoptic scale.

Orlanski scale	Spatial scale
Macro $\alpha$	10 000–40 000 km
Macro $\beta$	2000–10 000 km
Meso $\alpha$	200–2000 km
Meso $\beta$	20–200 km
Meso $\gamma$	2–20 km
Micro $\alpha$	200–2000 m
Micro $\beta$	20–200 m
Micro $\gamma$	2–20 m

ScanSAR wide mode, which has a swath width of approximately 500 km and a resolution of 100 m.

The SAR imagery presented herein have been smoothed from 100- to 600-m resolution in order to minimize the presence of small-scale oceanic signatures that may be confused with small-scale atmospherically induced signatures. Similar crude oceanic filtering methods have been employed by researchers attempting to create SAR-derived wind speed datasets (e.g., Monaldo et al. 2001). The price paid for this removal of oceanographic “clutter” is the elimination of some micro- $\alpha$ -scale atmospheric SAR signatures that could have provided insight into atmospheric boundary layer properties.

Large-scale oceanographic features can also produce corresponding signatures in SAR imagery. For example, many researchers have examined the SAR signature of the Gulf Stream North Wall (GSNW). The GSNW is made evident in SAR imagery by the buoyancy and air-sea momentum flux discontinuity that often accompanies it (e.g., Sikora et al. 1995; Beal et al. 1997). In the present research, we have carefully cross-referenced our SAR imagery with meteorological model analyses in order to ensure that our documented frontal signatures are atmospherically induced. In particular, we have relied heavily on the operational global analyses produced by the U.S. Naval Operational Global Atmospheric Prediction System (NOGAPS; Rosmond 1981), making use of the relative positioning of key features in the time-evolving fields of vector wind, pressure, temperature, temperature advection, and air-sea temperature difference. While the relatively coarse resolution of  $1^\circ$  latitude and longitude is insufficient to resolve scales below about meso- $\alpha$ , NOGAPS does have an advantage over existing high-resolution models in that it provided global coverage during the years spanned by our study. Higher-resolution model analyses can, of course, provide much greater insight when they are available. As is the case for the traditional observational data sources we quote, space limitations preclude us from presenting corresponding NOGAPS analyses for every SAR image contained herein.

Examination of this Alaska SAR Demonstration Project dataset and corresponding careful cross-referencing with NOGAPS global analyses yielded 158 cases of well-defined frontal signatures: 22 warm fronts, 37 cold fronts, three stationary fronts, 32 occluded fronts, and 64 secluded fronts. The latter are cases in which occluded fronts had wrapped around a low to form a closed seclusion. This frontal image collection forms the basis of the discussion below. All frequencies referred to therein are derived from this sample.

For presentation purposes, all of the SAR imagery in this paper were processed to remove the strong incidence angle trend present in HH-pol radar cross-section (RCS) imagery. The resulting grayscale images are related to backscatter and are hereafter referred to

as backscatter images. For each image, north is oriented toward the top of the page.

## 2. Discussion

### a. Generic frontal signatures in SAR imagery

Most synoptic-scale atmospheric fronts share two generic SAR-observable features. The first is a near-zero-order change in the mean backscatter while the second is a near-zero-order change in the character of the micro- $\alpha$ - to meso- $\gamma$ -scale eddy SAR signatures. The detection of these two features in a SAR image thus provides evidence for the existence and location of a synoptic-scale front. We note that large-scale oceanic fronts such as the GSNW can also force the same types of SAR signatures. Thus, when examining SAR imagery for the signatures of synoptic-scale atmospheric fronts in areas prone to oceanic fronts, the analyst must refer to synergistic data sources to ensure the signature of interest is indeed atmospherically induced.

The near-zero-order change in mean backscatter is typically of at least meso- $\beta$ -scale length, spanning most or all of a SAR image. In contrast, the width of the zone of strong backscatter gradient is much less, often meso- $\gamma$  to micro- $\alpha$ . Thus, this generic frontal SAR signature allows for precision in placement of front by the surface analyst beyond that which can be obtained using traditional data sources.

The mean backscatter discontinuity in Fig. 1a is typical of a well-defined synoptic-scale front, in this case an occluded front (frontal identification discussed below). This concentration of cross-frontal gradient is inherent in the frontogenetic process; a good working definition of a synoptic-scale front could, in fact, be *an elongated zone of significantly enhanced horizontal gradients of wind, temperature, or humidity resulting from deformation, shearing, tilting, or diabatic processes operating on the synoptic scale*. Because frontogenesis concentrates horizontal gradients of the vector wind, there is generally a change in wind direction, and often wind speed, across a front. Cross-frontal gradients in both quantities are apparent in Fig. 1b, the SeaWinds scatterometer wind vectors for this case obtained at 25-km resolution by the National Aeronautics and Space Administration's (NASA) Quick Scatterometer (QuikSCAT) instrument (Weissman et al. 2002). Depending on the wind-relative look angle of the SAR, these gradients will produce a corresponding gradient in backscatter and, hence, the SAR signature described above. It is possible, however, for these signatures to be masked when a chance combination of look angle and cross-front vector wind difference results in identical backscatter values for both sides of the front.

The same frontogenetic process that enhances vector wind gradients across fronts also concentrates the thermodynamic differences between adjacent air masses (Schultz et al. 1998). Thus there is typically a strong

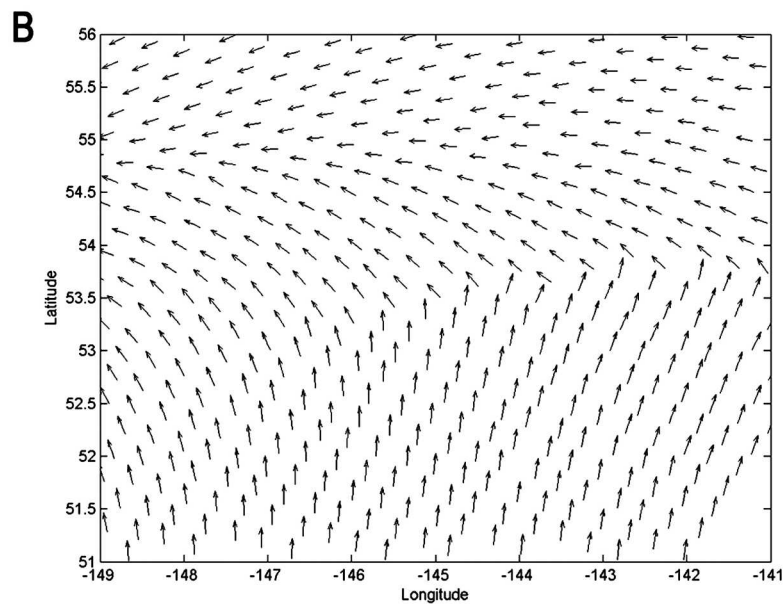
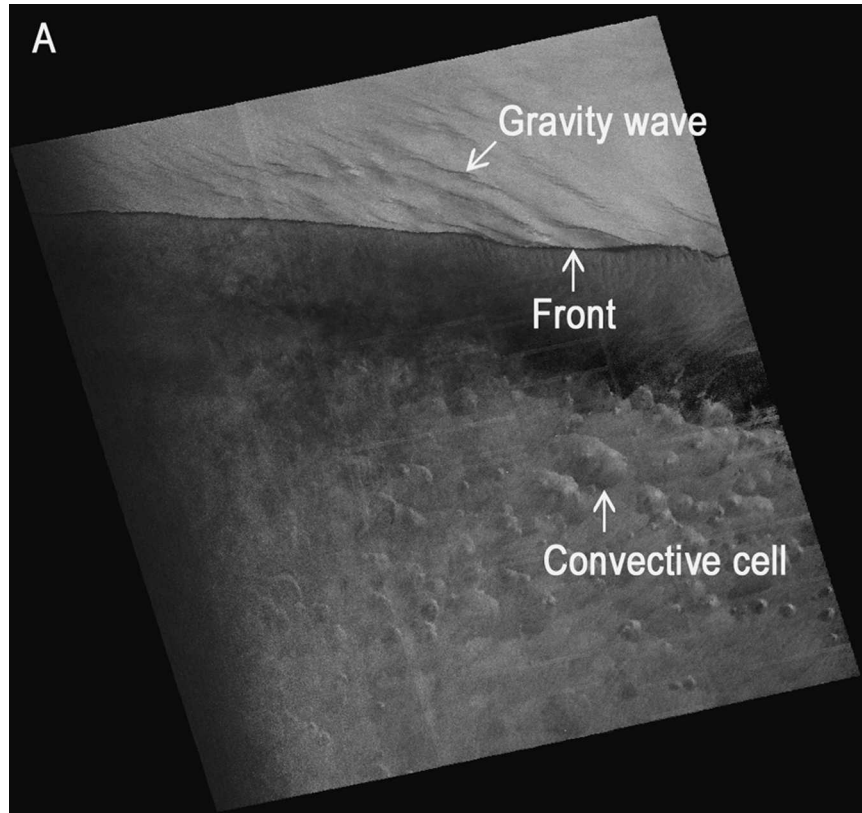


FIG. 1. (a) *RADARSAT-1* SAR image of a well-defined occluded front in the Gulf of Alaska at 0320 UTC 12 Jan 2003. The front is oriented east–west and moving toward the north. Image is located at 53°N, 144°W. (b) SeaWinds scatterometer wind vectors for the image region from revolution 18566, approximately 1 h later.

cross-frontal gradient in boundary layer temperature and a corresponding gradient in air–sea temperature difference (Neiman et al. 1990). If this stability change is sufficient to alter the type, scale, or intensity of

boundary layer turbulence, there can be a near-zero-order change in the character of the micro- $\alpha$ - to meso- $\gamma$ -scale eddy SAR signatures across the front. In this case, the analyst can use the existence of these features

to deduce the surface layer stability on both sides of the front; information that often allows one to infer the pattern of temperature advection and thus the frontal type.

Figure 1a provides an example of this effect, in this case gravity waves (e.g., Vachon et al. 1995; Winstead et al. 2002) embedded in the frontal inversion north of the surface front and convective outflows (e.g., Atlas and Black 1994; Babin et al. 2003) in the unstable air mass to the south of the surface front.

The gravity wave SAR signatures take the form of elongated bands of smooth variation in the SAR backscatter field, sometimes with a sharp discontinuity at one edge of each band as seen here. This pattern reflects the surface wind field induced by the gravity waves' pressure field and their vertical transport of momentum. Given the lack of nearby terrain, the gravity waves in this case are probably drawing their energy from the vertical shear across the frontal zone, that is, the thermal wind.

In contrast, the convective outflow SAR signatures often take the form seen here, with an arc-shaped leading gust fading to a trailing pool of lower wind speeds in a pattern reminiscent of that in downdraft-fed cold pools of much larger scale convective systems (Young et al. 1995). This pattern reflects the superposition of the divergent outflow under the convective downdraft upon the ambient wind field.

### *b. Recognizing frontal types in SAR imagery*

The subsequent sections will explore the SAR signatures that tend to differ between frontal types, allowing the SAR analyst to contribute to identification of fronts by type. This discussion will be limited to cold, warm, occluded, and secluded fronts because stationary fronts were rare in the Alaska SAR Demonstration dataset. Access to SAR images from the subtropics would eliminate this limitation and allow the extension of this analysis method to lower latitudes.

#### 1) COLD FRONTS

Because cold fronts advance as gravity currents (Young and Johnson 1984; Physick 1988), they often exhibit lobe and cleft instability (Simpson 1972; Lee and Wilhelmson 1997; Härtel et al. 2000). The resulting bulges in the surface front, convex in the direction of frontal motion and cusped toward the cold air, produce signatures in SAR images such as those in Figs. 2a,b and 3a. Such cusps are expected to form on any gravity current that propagates at a quasi-steady speed in a direction perpendicular to itself. The propagation increases the radius of curvature of frontal segments that bow away from the direction of propagation and reduces the radius of curvature for those segments that bow in the direction of propagation. Starting from an

initially perturbed front, this mechanism leads to a series of lobes (frontal segments bowed in the direction of propagation) and clefts (cusps in the front pointing away from the direction of propagation). The interesting issues are thus the origin and wavelength of the initial frontal perturbations (Härtel et al. 2000). Buoyant instability under the nose of the gravity current has been documented in laboratory (Simpson 1972) and theoretical studies (Härtel et al. 2000). The expected horizontal wavelength of such frontal instability is, however, less than the depth of the air mass (Simpson 1972; Lee and Wilhelmson 1997), suggesting that the resulting lobes and clefts should be markedly smaller than those seen in Figs. 2a,b and 3a. An alternative source of the initial perturbations is horizontal shear instability, as will be discussed below. For the Alaska SAR Demonstration dataset, 43% of cold fronts exhibit lobe and cleft instability as compared with 10% of other fronts. Thus, the existence of this bulge and cusp signature suggests that the corresponding SAR frontal signature is that of a cold front.

Another feature frequently observed in SAR imagery of cold fronts is the existence of a series of meso- $\gamma$ -scale vortices spaced along the frontal discontinuity. The creation of these small-scale vortices along the leading edge of gravity currents is abetted by the clefts acting as initiation points for vortex wrapup (Lee and Wilhelmson 1997; Parsons and Hobbs 1983), a process captured in the incipient and intermediate stages in Figs. 4a and 4b. Because cold fronts tend to exhibit a particularly narrow frontal zone and intense frontal lifting, a combination horizontal shear instability and stretching results in small but intense vortices. This intensity is enhanced because the frontal updraft tends to become concentrated in the frontal clefts (Härtel et al. 2000), right where the vortices form. The resulting circulation intensity is often sufficient to saturate SAR imagery as seen in Figs. 4a and 4b. These tightly wrapped vortices were observed only in cold fronts, and then only in about 1/3 of the cases. The most clear-cut examples are observed in the narrower fronts, but event and nonevent cases could not be distinguished based on cross-frontal jump in backscatter, width of the frontal zone, or a shear index computed as the ratio of the two. The importance of vortex stretching in the dynamics of this signature is reflected in the limited diagnostic power of these simple measures reflecting shear alone.

One of the rarest cold-front-specific SAR signatures is a series of front-parallel meso- $\gamma$ -scale backscatter bands resulting from Kelvin-Helmholtz instability behind the frontal head as seen in Fig. 5 (e.g., Young and Johnson 1984; Härtel et al. 2000). These front-parallel waves occur only when there is strong vertical shear of the cross-frontal wind component so they are endemic to fronts that behave as gravity currents, that is, cold fronts and smaller-scale phenomena such as gust fronts

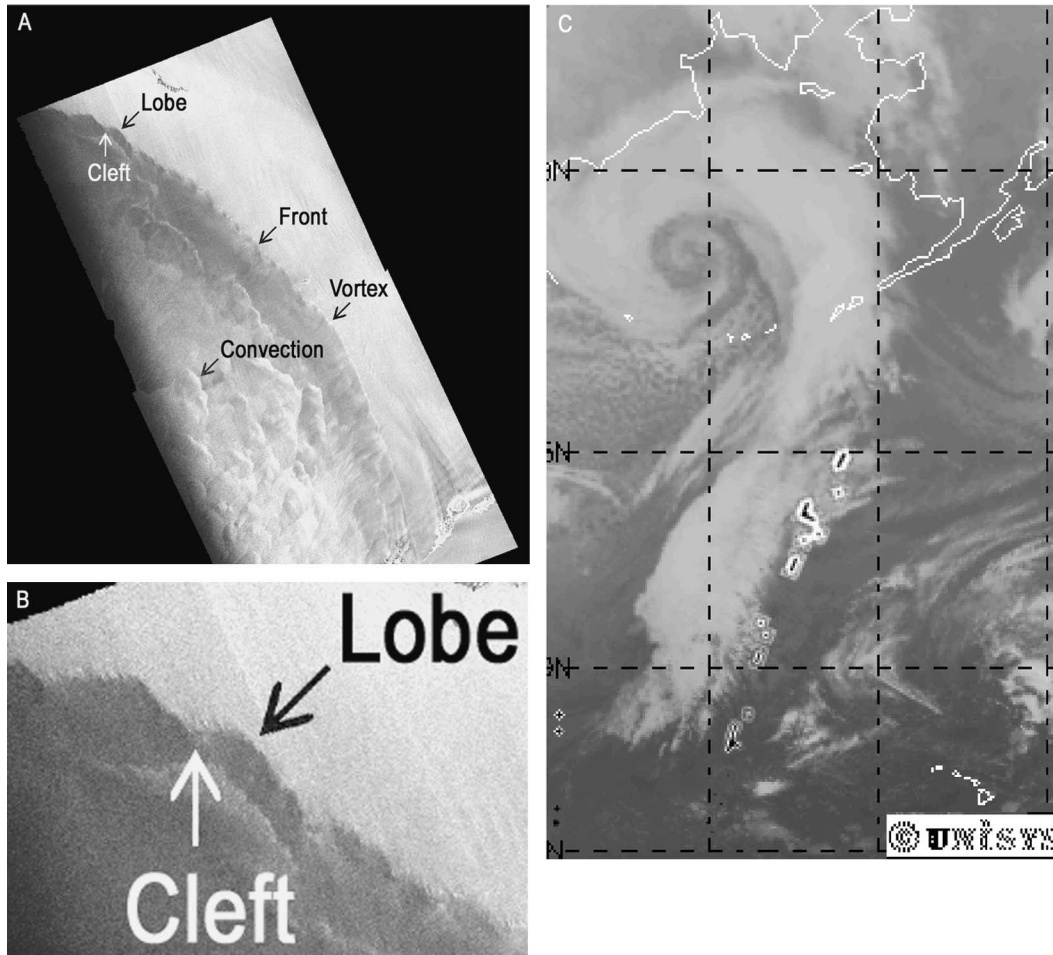


FIG. 2. (a) *RADARSAT-1* SAR image of an intense cold front moving through the Aleutian Islands at 0506 UTC 8 Feb 2001. The front is oriented northwest–southeast and moving toward the northeast. Image is located at 58°N, 172°W. (b) Zoomed SAR image showing detail of lobe and cleft structure. (c) GOES IR image from 2345 UTC 7 Feb 2001. (Courtesy of UNISYS.)

and sea breezes. The SAR signature is similar to that for an undular bore or a solitary wave packet (e.g., Alpers and Stilke 1996); therefore, other factors must be considered when using this feature to diagnose frontal type.

We point out that the three mesoscale features we described above as being associated with cold fronts are not usually detectable using traditional observational data sources because of their small scale and because they are often masked by upper-level clouds. None of the complementary data sources available to us for this study sensed the presence of the mesoscale features outlined above.

Some complementary data sources can, however, detect the presence of static stability changes across fronts, thus serving to confirm the analyst's interpretation of the SAR signatures of boundary layer eddies. An intense cold front will often exhibit a clear-cut SAR

signature of a cross-frontal stability change, with a rather homogeneous backscatter pattern in the near-neutral-stratification atmosphere ahead of the front and strong modulation of backscatter by convective downdrafts in the more-unstable boundary layer behind the front. Figures 2a and 4a provide particularly striking examples of meso- $\beta$ -scale convective downdraft signatures behind a cold front while Fig. 3a exhibits weaker and smaller-scale downdraft signatures. The difference in scale is probably related to a difference in the depth of the convective layer (Sikora et al. 1995, 1997) and perhaps the existence of evaporative enhancement of downdrafts in the deeper, larger-scale examples (Atlas and Black 1994).

Only cold front cases were observed to exhibit these convective SAR signatures *immediately* to the cold side of the front, and then only 30% of the time. (On occasion, occluded and secluded front cases had convective

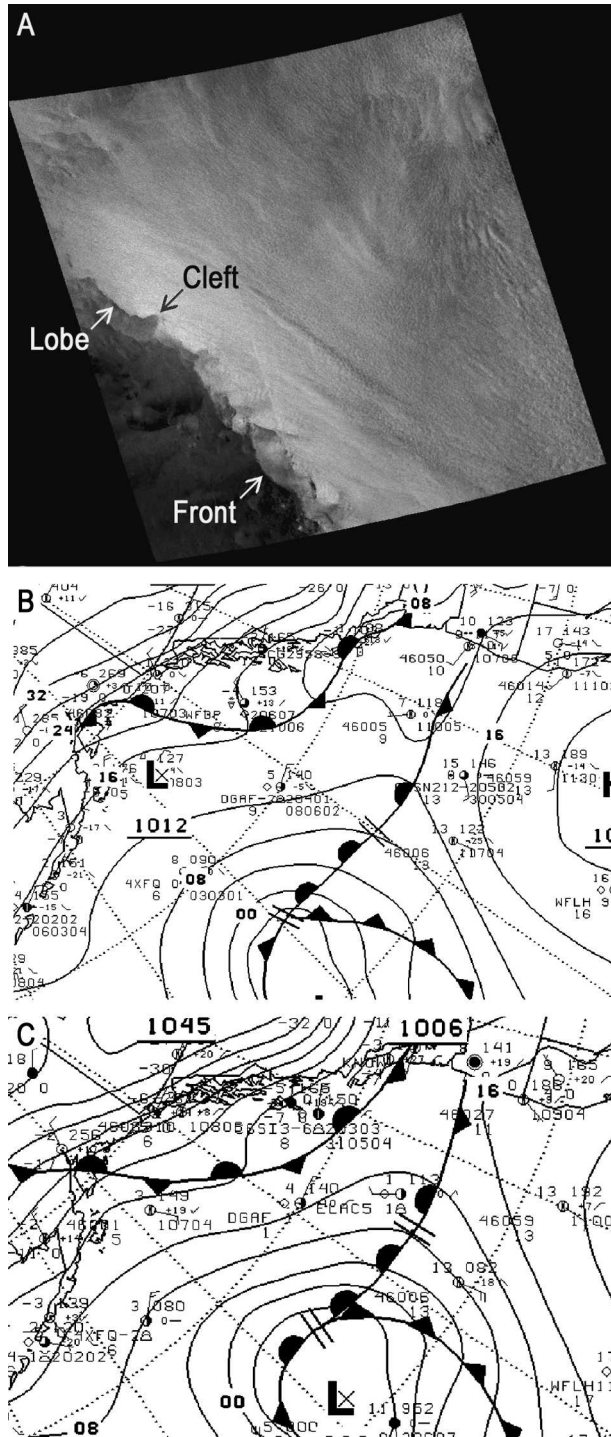


FIG. 3. (a) *RADARSAT-1* SAR image of a cold front in the Gulf of Alaska 0317 UTC 8 Mar 2003. The front is oriented northwest-southeast and moving toward the southwest. Image is located at 56°N, 144°W. (b) NCEP surface analysis valid 0000 UTC 8 Mar 2003. (c) NCEP surface analysis valid at 0600 UTC 8 Mar 2003.

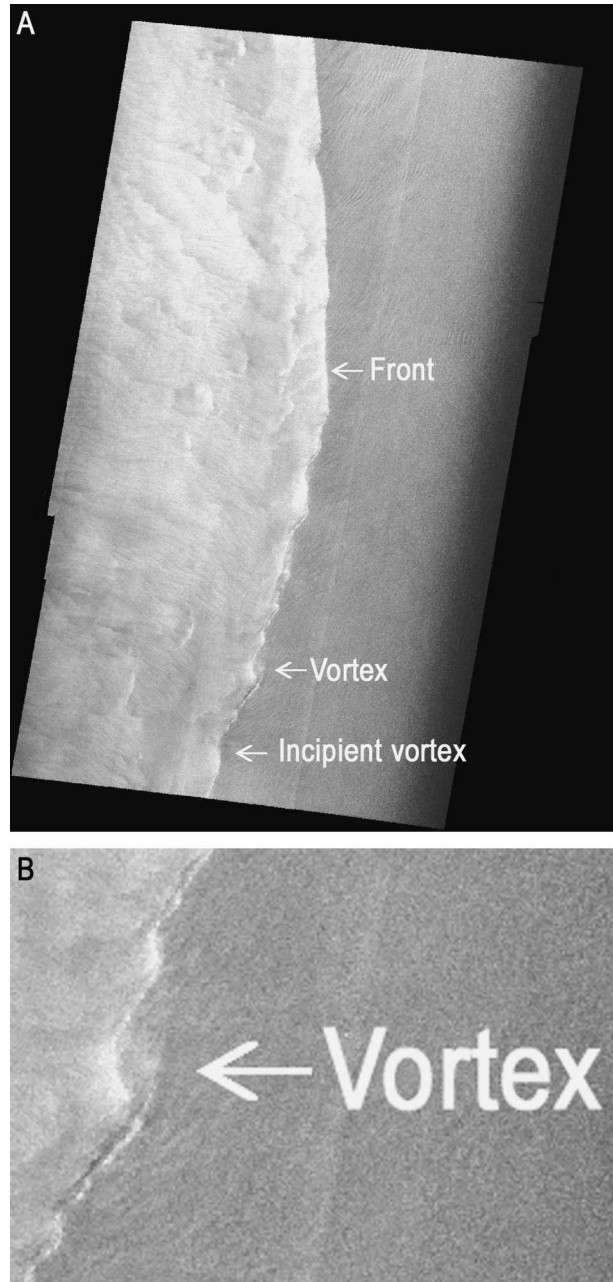


FIG. 4. (a) *RADARSAT-1* SAR image of a cold front in the Gulf of Alaska at 1545 UTC 20 Dec 2001. The front is oriented north-south and moving toward the east. Image is located at 47°N, 143°W. (b) Zoomed SAR image showing detail of vortex structure.

signatures but they were displaced a meso- $\beta$ -scale distance to the cold side of the front.) That these results are regionally biased can be seen by considering the postfrontal stability for cold-air outbreaks off the east coast of North America. The likelihood of convection could vary from near zero to almost 100% depending on season and thus the continent – ocean temperature

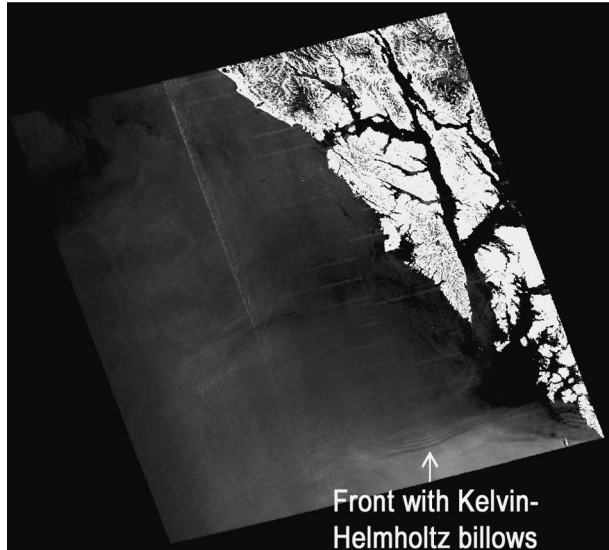


FIG. 5. *RADARSAT-1* SAR image of Kelvin–Helmholtz billows behind the head of a cold front off the Alexander Archipelago of southern Alaska at 0248 UTC 25 May 2002. The front is oriented east–west and moving toward the south. Image is located at 56°N, 137°W.

difference (Young and Sikora 2003). Thus, this SAR signature appears to reflect the existence of strong cold advection in the immediate rear of the front. The NOGAPS analyses corresponding to Figs. 2a and 4a capture both the cold advection and the resulting destabilization of the atmospheric boundary layer. Likewise, the postfrontal convection is clearly resolved by IR imagery from the National Oceanic and Atmospheric Administration Geostationary Operational Environmental Satellites (GOES; Fig. 2c), supporting the SAR interpretation. While this case highlights the success of IR imagery in capturing the static stability change associated with a cold front, it also illustrates the limitations of in situ observations for open-ocean frontal analysis. The only moored buoy in position to sample this event (National Data Buoy Center buoy 46035) ceased operation for the year in the midst of building seas and southwest winds gusting to gale force as the front approached.

Finally, the contribution of SAR to cold frontal analysis can be seen by comparing Fig. 3a to the corresponding sequence of National Centers for Environmental Prediction (NCEP) Pacific surface analyses (Figs. 3b,c). The surface analyses show a stationary (sic) front moving southwestward through the SAR image as the northeast winds of an arctic outbreak bring falling temperatures and rising pressures to the offshore region. The conventional surface observations were insufficient to allow NCEP to confirm this feature as a cold front. In contrast, the mesoscale SAR signatures associated with the front make the frontal type obvious given our discussion above.

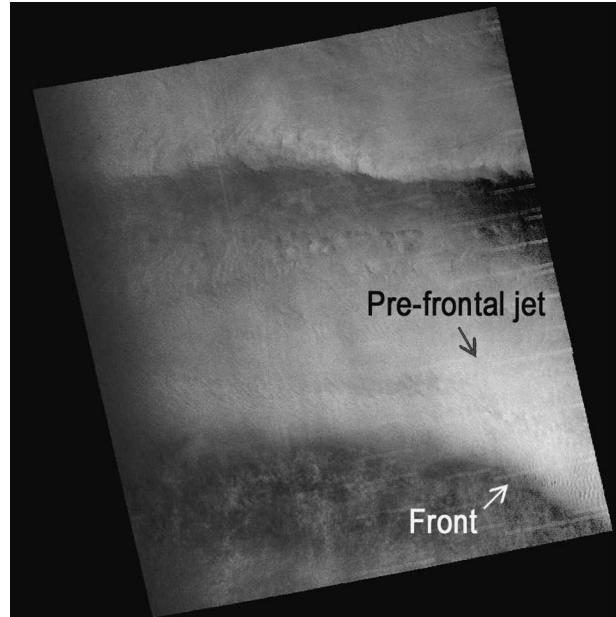


FIG. 6. *RADARSAT-1* SAR image of a warm front with pre-frontal jet to its north, Gulf of Alaska, at 0313 UTC on 3 Oct 2001. The front is oriented east–west in the western part of the image, turning gradually northwest–southeast in the eastern part of the image. It is moving to the north and northeast. Image is located at 56°N, 143°W.

## 2) WARM FRONTS

SAR signatures of warm frontal boundaries (e.g., Fig. 6) are typically much smoother than those of cold fronts and are often accompanied by the SAR signature of a prefrontal jet [i.e., conveyor belt; Carlson (1980)] that contributes to the cross-frontal gradient in SAR backscatter. Higher backscatter is found ahead of the front as captured in Fig. 6.<sup>1</sup> Conveyor belts with a pronounced maximum in backscatter paralleling the front were observed in 50% of the warm fronts, 33% of the secluded fronts, 31% of the occluded fronts, and only 10% of the cold fronts. The limited scale of SAR imagery may seriously impact these statistics, as may the high-latitude oceanic region from which most of the analyzed images came. Because of the frequency of cut-off lows in the Gulf of Alaska, the most common form of conveyor belt is associated with a band of cloudiness extending north from the midlatitudes and wrapping cyclonically around an occluded cyclone as IR imagery from the GOES satellites suggests is the case for Fig. 2c.

<sup>1</sup> The second band of enhanced backscatter at the top of the image appears unrelated to the front although it is confirmed by scatterometer, MM5, and NOGAPS surface wind fields (not shown). The NOGAPS and NCEP Pacific surface analyses (not shown) suggest that it is the result of an along-coast surge of cool air from the maritime polar high to the southeast.

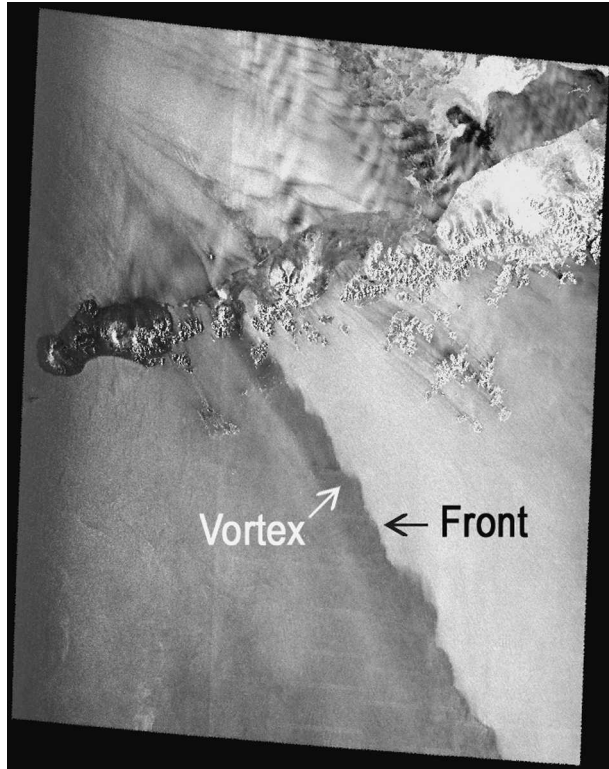


FIG. 7. RADARSAT-1 SAR image of a warm front with meso- $\beta$ -scale vortices near the Aleutian Islands at 0429 UTC 5 Feb 2000. The front is oriented northwest-southeast and moving toward the northeast. Image is located at 54°N, 162°W.

In this case, the broader view provided by IR imagery allows one to connect the prefrontal wind speed enhancement with the characteristic cloud pattern of a warm conveyor belt, thus confirming the frontal type deduced from SAR. In regions where traveling wave cyclones dominate, conveyor belts in association with cold fronts (i.e., warm conveyor belts) become more common (Carlson 1980).

Warm frontal signatures in SAR imagery often meander in response to meso- $\beta$ -scale vortices (e.g., Fig. 7). Warm fronts exhibit waviness on this scale 18% of the time, occluded fronts 12%, secluded fronts 9%, and cold fronts only 3%. Fronts that exhibit these vortices tend to be narrower than those without vortices but have similar cross-frontal differences in backscatter, suggesting that the cross-frontal shear is stronger. Thus, it is likely that these meso- $\beta$ -scale frontal waves result from horizontal shear instability (Martin 1996); a hypothesis in keeping with the conveyor belt statistics discussed above.

Another SAR signature of shear across the frontal zone is the existence of meso- $\gamma$ - or micro- $\alpha$ -scale banding aligned nearly perpendicular to the front. When present, such bands usually extend only a few 10s of kilometers to the cold side of the front as in Fig. 8a.

Given their smoothness and association with a strong conveyor belt, it is conjectured that they reflect shear-driven gravity waves in the frontal inversion. Similar SAR signatures have been documented for terrain-driven gravity waves in a frontal inversion, wherein they also faded as the frontal inversion is lifted farther from the surface (Winstead et al. 2002). Of potential dynamic interest is the apparent modulation of such gravity waves by horizontal shear instability waves as exhibited in Fig. 8a.

Occasionally the SAR image may be placed so as to allow the intersection of the warm and cold conveyor belts to be observed as in Fig. 9. When present, this overrunning SAR signature allows the analyst to distinguish the warm front from its occluded extension.

The potential for synergy between SAR and a broad range of conventional data sources is well illustrated by the case shown in Fig. 8a. The NCEP Pacific surface analyses (not shown) depict a warm front moving through the SAR image, suggesting successful synthesis of the available non-SAR information. The model analyses [the Aviation Model (AVN) and NOGAPS] reveal that the front lies along a deformation zone between northerlies and southerlies, west of the col and east of a triple point where it intersects a cold front. These features support the NCEP designation of a warm front. The SeaWinds scatterometer (Fig. 8b) also captures this combination of features and depicts the front in the same position and orientation as SAR. The scatterometer's resolution prevents it, however, from sensing the gravity waves apparent in the SAR image. Thus, what SAR brings to this mix is an ability to locate the front with a high degree of precision and support for the other sensors by typing the front based on its meso- $\gamma$ -scale features.

### 3) OCCLUDED FRONTS

Occluded fronts may have SAR-observable features in common with warm fronts, making them hard to distinguish on the basis of SAR imagery alone. As with warm fronts, occluded fronts are generally smooth except where they meander in response to meso- $\beta$ -scale vortices. Moreover, front-perpendicular gravity wave SAR signatures are also observed with some occluded fronts as seen in Fig. 10a. Occasionally the gravity waves are oriented at more acute angles to the front as in Fig. 1. Gravity wave SAR signatures are about 50% (22% versus 14%) more common in occluded fronts than in warm fronts, perhaps reflecting the strong vertical shear associated with the conveyor belt wrapping into the major occluded cyclones of the Gulf of Alaska. As mentioned earlier, SAR is a valuable tool for the recognition of such features as they are too small to be resolved by traditional datasets, such as the SeaWinds scatterometer data (Fig. 10b).

One feature that can help distinguish occluded from

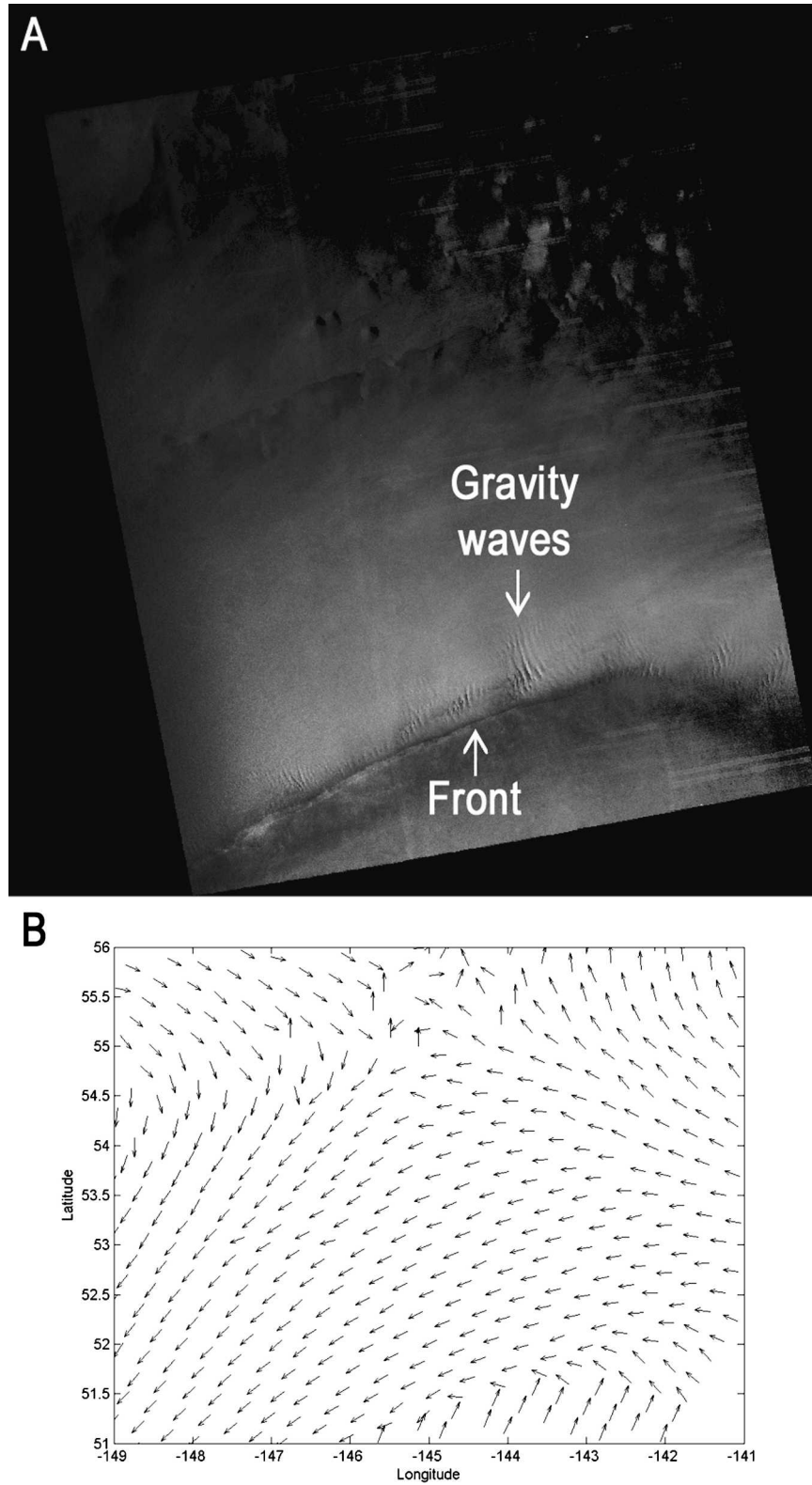


FIG. 8. (a) *RADARSAT-1* SAR image of a warm front with gravity waves in the Gulf of Alaska at 0320 UTC 30 Mar 2002. The front is oriented southwest–northeast and moving toward the northwest. Image is located at 53°N, 144°W. (b) SeaWinds scatterometer wind vectors for the image region from revolution 14460, approximately 1 h later.

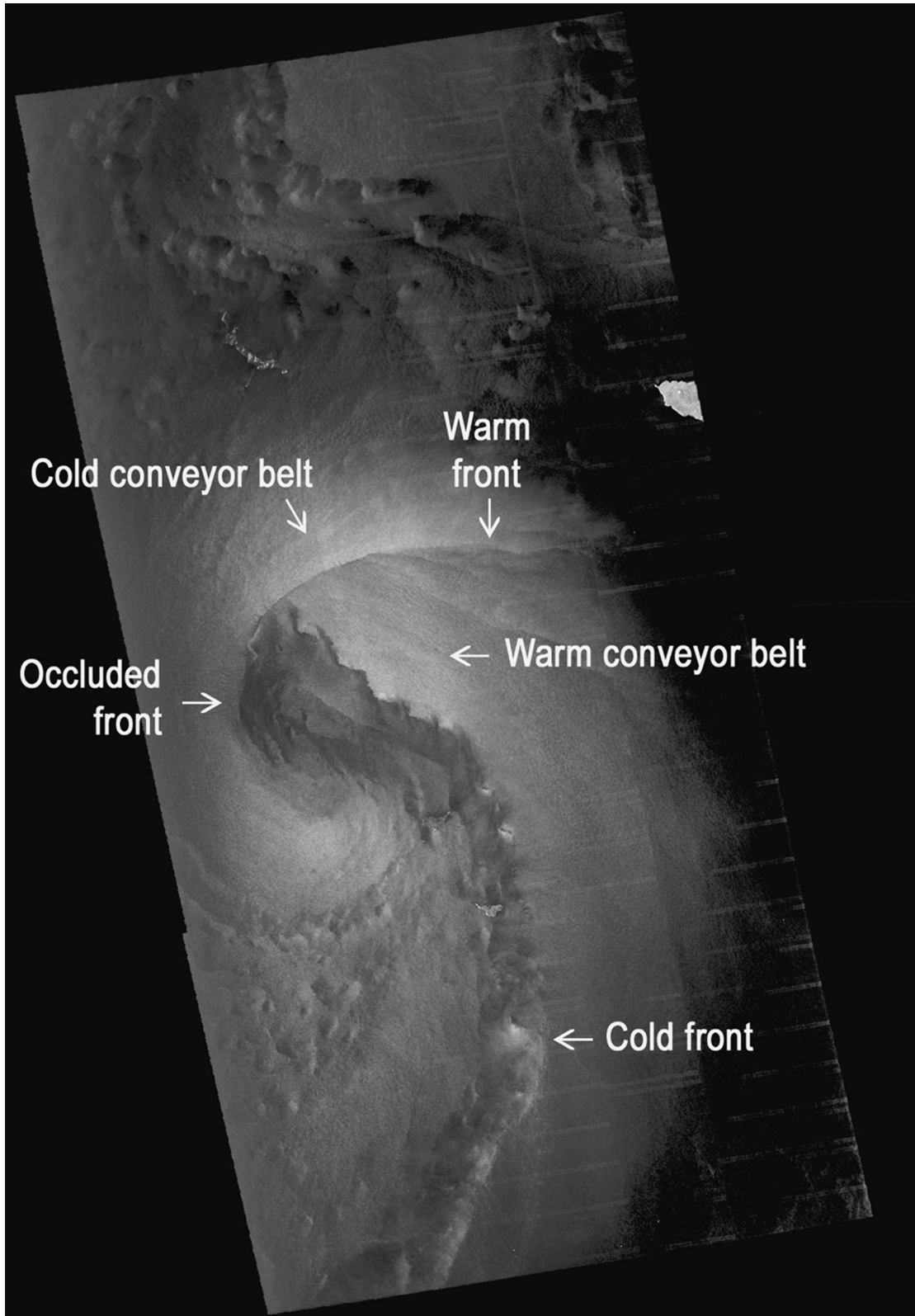


FIG. 9. *RADARSAT-1* SAR image of the intersection of the warm and cold conveyor belts in the Bering Sea at 0500 UTC 31 Oct 1999. The fronts are labeled in the image and are moving counterclockwise around the low, which is located near the center of the image. Image is located at 56°N, 169°W.

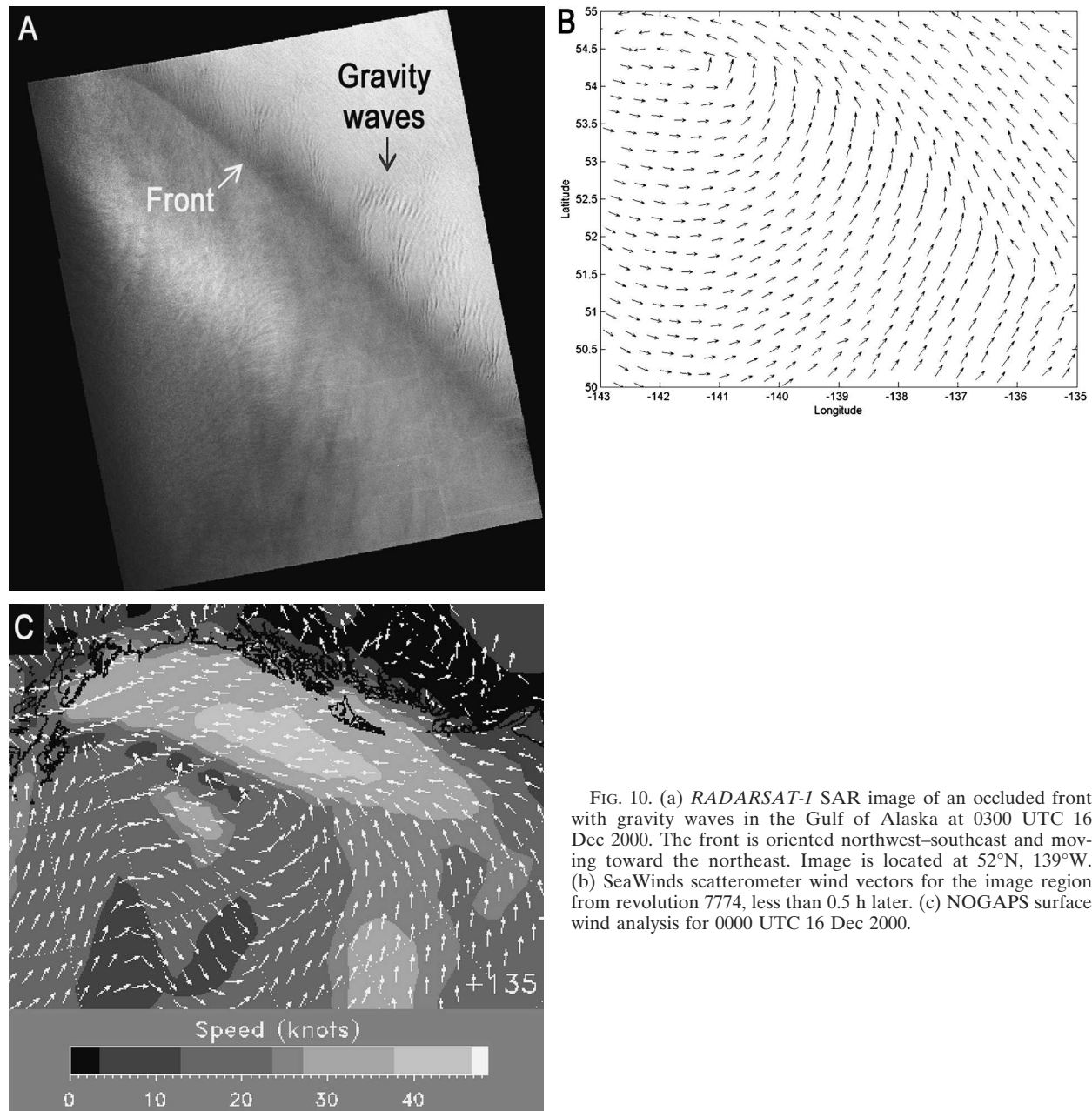


FIG. 10. (a) *RADARSAT-1* SAR image of an occluded front with gravity waves in the Gulf of Alaska at 0300 UTC 16 Dec 2000. The front is oriented northwest-southeast and moving toward the northeast. Image is located at 52°N, 139°W. (b) SeaWinds scatterometer wind vectors for the image region from revolution 7774, less than 0.5 h later. (c) NOGAPS surface wind analysis for 0000 UTC 16 Dec 2000.

warm fronts is the width of the backscatter gradient. This zone of changing wind speed and direction averages about twice as wide for the observed occluded fronts as for warm fronts. Because the cross-front backscatter differences are similar for these three frontal types, it is possible that cross-front shear is weakest for occluded fronts. Combined with the indications that vertical shear is greatest in these fronts, this result is suggestive of differences in frontal slope. Such differences cannot, however, be verified without in situ upper-air observations.

The synoptic setting remains, however, the best way

to distinguish occluded from warm fronts. Patterns of thermal advection can be particularly useful. The NOGAPS analysis (Fig. 10c), for example, shows the frontal trough lying along the southwest edge of an intense conveyor belt, just northwest of where it is intersected by a second belt from the southwest. This pattern suggests the intersection of warm and cold fronts to form an occluded front. The NCEP Pacific surface analysis (not shown) supports this interpretation. Similarly, the SeaWinds scatterometer (Fig. 10b) shows the front and conveyor belt in the same positions as SAR and enough other features [occluded front

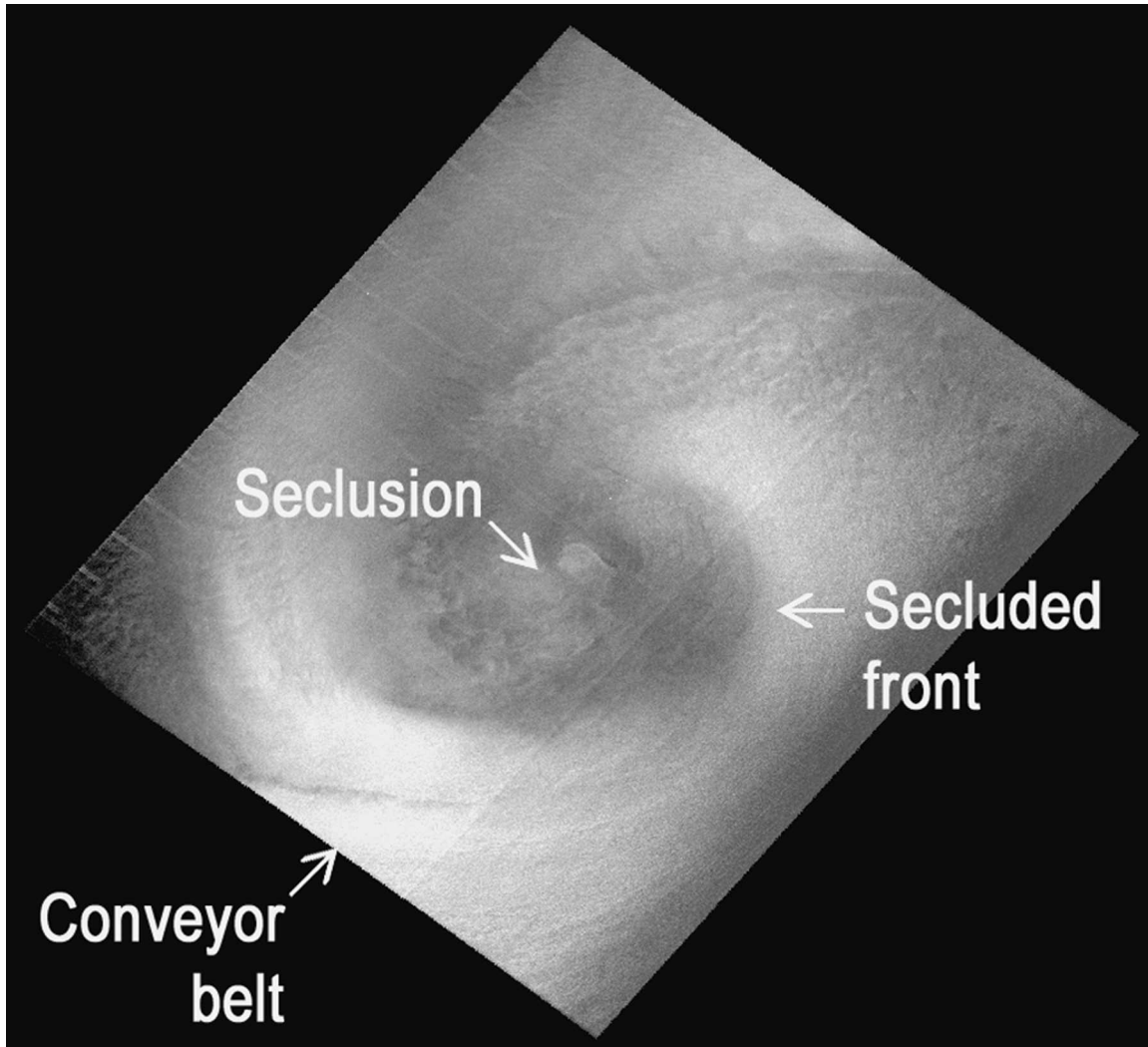


FIG. 11. *RADARSAT-1* SAR image of a secluded front in the Bering Sea at 1818 UTC 6 Dec 2000. Image is located at 55°N, 175°W.

(identification discussed below), cold front, warm front] to make it clear that this is an occluded front.

#### 4) SECLUDED FRONTS

As occluded cyclones continue to evolve, the tip of the occluded front sometimes wraps into a ring leading to the seclusion stage of cyclone development (e.g., Kuo et al. 1992; Neiman and Shapiro 1993; Neiman et al. 1993; Chang et al. 1996). The resulting secluded front often has a surrounding low-level jet (an extension of the cold conveyor belt) with a tight radius of curvature (Fig. 11). While existing theoretical and modeling studies suggest that the surface air in the center of these seclusions is warmer than that in the surrounding conveyor belt (e.g., Chang et al. 1996; Kuo et al. 1992), the NOGAPS analysis sometimes indicates the existence of a cold core at the surface. Because there ap-

pears to be SAR-detectable differences between the warm-core and cold-core cases, they will be distinguished below and a SAR-supported conjecture about their origin will be presented. Thus, based on the NOGAPS-analyzed surface temperature field, seclusions will be divided into three categories: warm, cold, and indeterminate. Circumseclusion conveyor belts with a notable falloff in backscatter farther out from the seclusion occur in 42% of warm seclusions, 36% of cold seclusions, and less than 33% of indeterminate seclusions. Thus, these conveyor belts are roughly as common as those ahead of warm fronts and occluded fronts. This result is in keeping with their formation as the downwind extension of a preexisting cold conveyor belt (e.g., Kuo et al. 1992; Neiman and Shapiro 1993).

Secluded fronts also exhibit occasional cross-frontal differences in boundary layer SAR signatures, but of a pattern more complex than that observed with cold

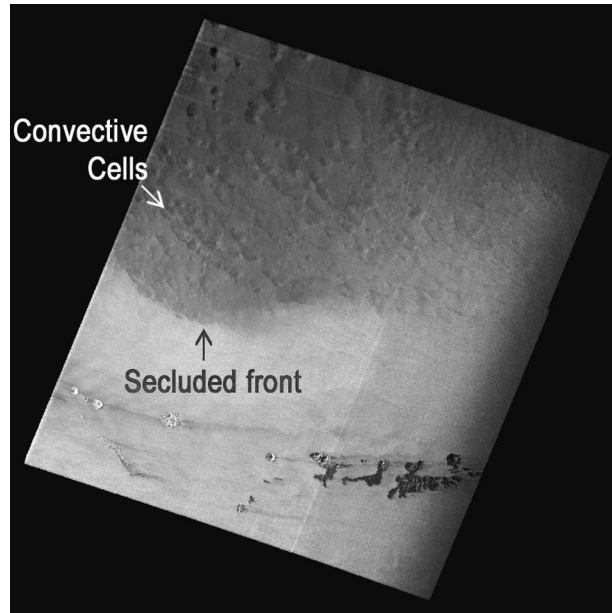


FIG. 12. *RADARSAT-1* SAR image of a secluded front north of the Aleutian Islands at 1810 UTC 16 Nov 2002. Image is located at 53°N, 176°W.

fronts. Rather than the instability starting immediately to the cold side of the front, the onset of convective SAR signatures is displaced radially outward 100–200 km from the secluded front. This pattern was observed in 15% of warm seclusions, 11% of cold seclusions, and 13% of indeterminate seclusions. It is conjectured that secluded fronts exhibiting this behavior are embedded in the generally unstable environment of a cold-core cutoff low and further that it is the combination of low frontal inversion and warm advection in the trough of warm air aloft (Martin 1999) that prevents the formation of convective SAR signatures in the 100–200 km closest to the front. Mesoscale modeling or in situ upper-air observations would be required to verify this hypothesis.

Most seclusions exhibit well-defined backscatter fronts surrounding a low wind core as seen in Figs. 11, 12, and 13a. This backscatter gradient is often sharper in warm seclusions than in cold seclusions. Some 9% of warm seclusions exhibit mesoscale convective SAR signatures within the low wind core as captured in Fig. 12; cold seclusions have not been observed to do so. This difference suggests that the SAR signatures are caused by convective mixing of air from the elevated cold core of the parent cutoff low with warm boundary layer air trapped within the seclusion. Over time, this convective redistribution of heat could result in the extension of the cold core aloft to the surface replacing the advectively created warm core of the seclusion. It is hypothesized that this effect is responsible for the cold cores analyzed by NOGAPS for some seclusions, with the coldness of the midlevels being the deciding factor.

Seclusions differ from occluded fronts in that both warm and cold seclusions have about a 10% likelihood of exhibiting gravity wave SAR signatures, about half that for occluded fronts. Other features are, however, quite similar. Neither seclusions nor occlusions exhibit lobe and cleft instability and both have similar odds of exhibiting meso- $\beta$ -scale waves (11% and 12%, respectively).

Research-grade satellite imagery and model output can sometimes be used to confirm the SAR interpretation as in Fig. 13a. Moderate Resolution Imaging Spectroradiometer (MODIS; King et al. 1992) imagery (Fig. 13b) from NASA's *Terra* spacecraft 5 h and 25 min after the SAR image (Fig. 13a) reveal a mix of cirrus and what is either altocumulus or stratocumulus with no sign of deep precipitating convection. Likewise, the University of Washington fifth-generation Pennsylvania State University–National Center for Atmospheric Research Mesoscale Model (MM5) surface analysis (Fig. 13c) for 1 h and 30 min after the SAR image shows only a degree or two of warming in the seclusion. Moreover, the mesoscale model (6 h into the forecast to allow time for spinup of mesoscale detail) captures the sharp wind shift seen in the SAR imagery southwest of the seclusion and suggests that this feature may be associated with a secondary cold front, something that would be difficult to deduce from SAR imagery alone because of the limited image size.

### 3. Conclusions

Synthetic aperture radar imagery offers much better spatial resolution than other currently flying spaceborne remote sensors. SAR's resolution is an order of magnitude greater than that for operational cloud imaging satellites and two orders of magnitude greater than that for other surface wind imaging satellites. We argue that the incorporation of SAR into the marine analyst's toolbox would greatly facilitate the finescale analysis of atmospheric fronts at sea. The basis for this assertion comes from our analysis of some 6000 *RADARSAT-1* SAR images from the Alaska SAR Demonstration dataset. This analysis yielded 158 cases of well-defined frontal signatures: 22 warm fronts, 37 cold fronts, three stationary fronts, 32 occluded fronts, and 64 secluded fronts. In the preceding discussion, we show how each category of front is typically distinguishable from the others, and we point out common SAR-observable finescale structures associated with each category of front.

Primary drawbacks to the operational use of SAR imagery in the preparation of finescale marine analyses are its limited cross-track spatial coverage in any one scene and its low-frequency repeat cycle. These problems can be addressed by the development of wide-swath SAR modes and the launch of more satellites bearing SARs. The outlook for such, as shown in

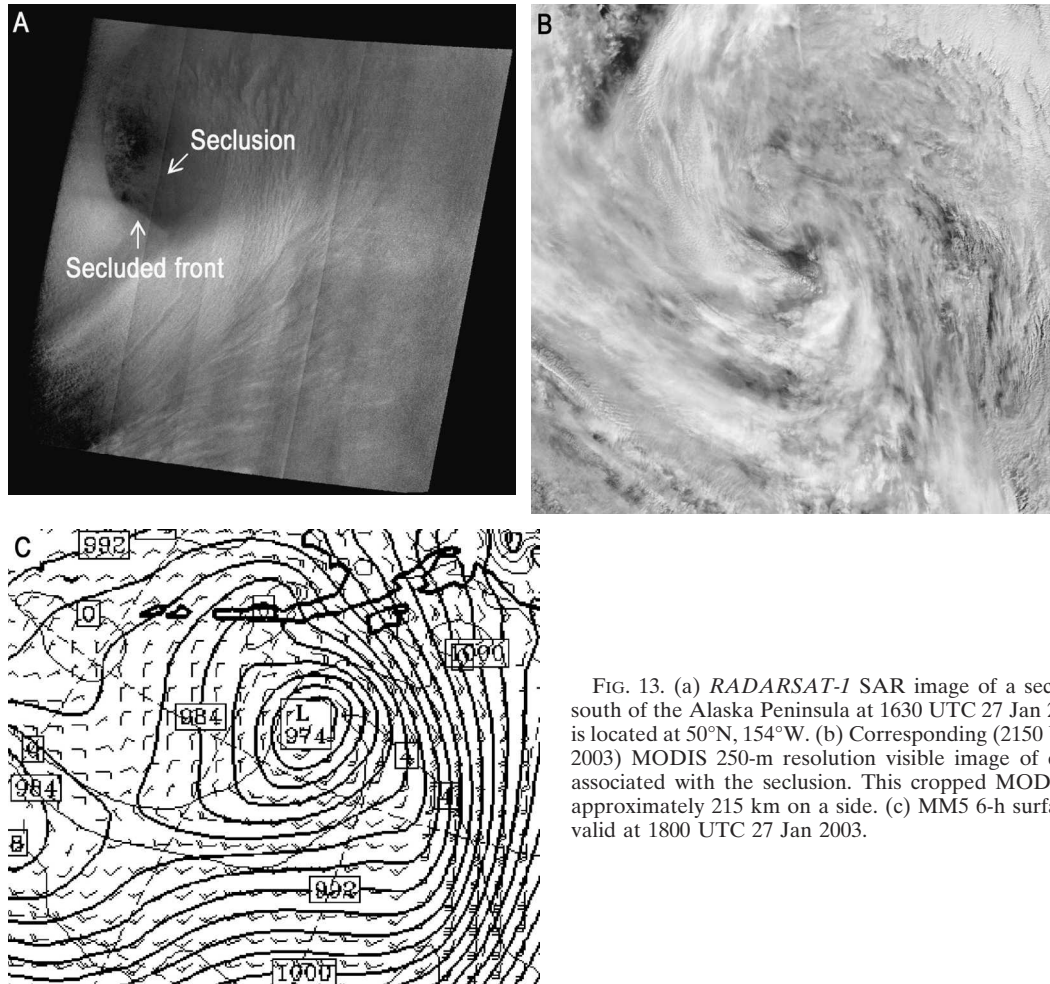


FIG. 13. (a) RADARSAT-1 SAR image of a secluded front south of the Alaska Peninsula at 1630 UTC 27 Jan 2003. Image is located at 50°N, 154°W. (b) Corresponding (2150 UTC 27 Jan 2003) MODIS 250-m resolution visible image of cloud cover associated with the seclusion. This cropped MODIS image is approximately 215 km on a side. (c) MM5 6-h surface forecast valid at 1800 UTC 27 Jan 2003.

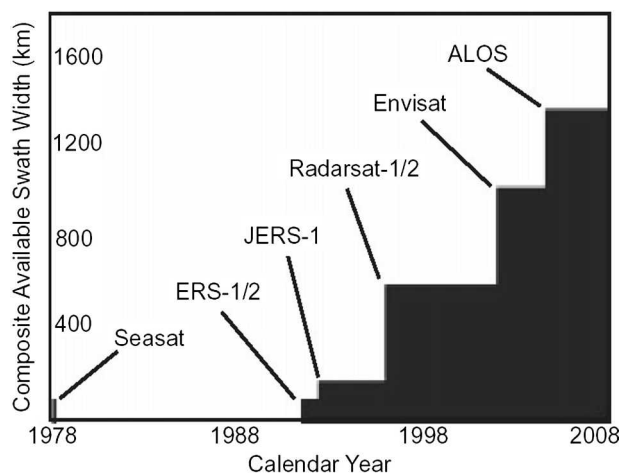


FIG. 14. Swath width as a function of year for existing and proposed synthetic aperture radar satellites.

Fig. 14, is optimistic (Beal et al. 2003). Until such time as additional wide-swath SARs join the constellation, SAR-based analyses serve primarily to provide insight into the structure and behavior of weather systems, information that that can subsequently be used to forecast the impacts of similar systems observed by other means. Issues addressable with the current generation of SAR datasets include the space and time climatology of the various subsynoptic-scale frontal structures discussed above, the relationship between these frontal structures and cloud features (using geosynchronous satellite cloud imagery), and possibly the discovery of new phenomena such as the near-front surface SAR signatures of shear-driven gravity waves. These and equivalent studies of other marine meteorological phenomena require the widespread availability of SAR backscatter imagery, an issue that is contingent upon the data policy of those funding and administering SAR satellites.

*Acknowledgments.* This work was supported in part by Grant ATM0240869 from the National Science

Foundation and Grants N00014-04-539, N00014-03-WR-20329, and N00014-04-WR-20365 from the Office of Naval Research. RADARSAT data shown in Figs. 1–13 courtesy of the Canadian Space Agency; processed and distributed by RADARSAT International. The SAR imagery shown in this paper were provided by the National Oceanic and Atmospheric Administration's Ocean Remote Sensing Program via the Alaska SAR Demonstration Project. Results from the University of Washington's real-time mesoscale model were provided by Mark Albright

## REFERENCES

- Alpers, W., and G. Stilke, 1996: Observation of a nonlinear wave disturbance in the marine atmosphere by synthetic aperture radar aboard the *ERS-1* satellite. *J. Geophys. Res.*, **101**, 6513–6525.
- Atlas, D., and P. Black, 1994: The evolution of convective storms from their footprints on the sea as viewed by synthetic aperture radar from space. *Bull. Amer. Meteor. Soc.*, **75**, 1183–1190.
- Babin, S. M., T. D. Sikora, and N. S. Winstead, 2003: A case study of satellite synthetic aperture radar signatures of spatially evolving atmospheric convection over the western Atlantic Ocean. *Bound.-Layer Meteor.*, **106**, 527–546.
- Beal, R. C., P. S. DeLeonibus, and I. Katz, Eds., 1981: *Spaceborne Synthetic Aperture Radar for Oceanography*. The Johns Hopkins University Press, 215 pp.
- , V. N. Kudryavtsev, S. A. Grodsky, D. G. Tilley, V. A. Dulov, and H. C. Graber, 1997: The influence of the marine atmospheric boundary layer on *ERS-1* synthetic aperture radar imagery of the Gulf Stream. *J. Geophys. Res.*, **102**, 5799–5814.
- , G. S. Young, F. Monaldo, D. Thompson, N. Winstead, and C. Scott, cited 2003: High resolution wind monitoring with wide swath SAR: A user's guide. The Johns Hopkins University Applied Physics Laboratory. [Available online at [http://fermi.jhuapl.edu/sar/stormwatch/user\\_guide/](http://fermi.jhuapl.edu/sar/stormwatch/user_guide/)]
- Bosart, L. F., 2003: Whither the weather analysis and forecasting process? *Wea. Forecasting*, **18**, 520–529.
- Carlson, T. N., 1980: Airflow through midlatitude cyclones and the comma cloud pattern. *Mon. Wea. Rev.*, **108**, 1498–1509.
- Chang, S. W., T. R. Holt, and K. D. Sashegyi, 1996: A numerical study of the ERICA IOP 4 marine cyclone. *Mon. Wea. Rev.*, **124**, 27–46.
- Friedman, K. S., T. D. Sikora, W. G. Pichel, P. Clemente-Colon, and G. Hufford, 2001: Using spaceborne synthetic aperture radar to forecast polar mesoscale cyclones in the Bering Sea. *Wea. Forecasting*, **16**, 270–276.
- Härtel, C., E. Meiburg, and F. Necker, 2000: Analysis and direct numerical simulation of the flow at a gravity current head. Part 2: The lobe and cleft instability. *J. Fluid Mech.*, **418**, 213–229.
- Horstmann, J., H. Schiller, J. Schulz-Stellenfleth, and S. Lehner, 2003: Global wind speed retrieval from SAR. *IEEE Trans. Geosci. Remote Sens.*, **41**, 1437–1446.
- Jackson, C. R., and J. R. Apel, Eds., 2004: *Synthetic aperture radar marine user's manual*. NOAA/NESDIS/Center for Satellite Application and Research, Washington, DC, 455 pp.
- King, M. D., Y. J. Kaufman, W. P. Menzel, and D. Tanre, 1992: Remote-sensing of cloud, aerosol, and water-vapor properties from the Moderate Resolution Imaging Spectrometer (MODIS). *IEEE Trans. Geosci. Remote Sens.*, **30**, 2–27.
- Kuo, Y.-H., R. J. Reed, and S. Low-Nam, 1992: Thermal structure and airflow in a model simulation of an occluded marine cyclone. *Mon. Wea. Rev.*, **120**, 2280–2297.
- Lee, D. L., and R. B. Wilhelmson, 1997: The numerical simulation of non-supercell tornadogenesis. Part I: Initiation and evolution of pretornadic misocyclone circulations along a dry outflow boundary. *J. Atmos. Sci.*, **54**, 32–60.
- Martin, J. E., 1999: Quasigeostrophic forcing of ascent in the occluded sector of cyclones and the trowal airstream. *Mon. Wea. Rev.*, **127**, 70–88.
- Martin, R. F., 1996: Observations of 250-km-wavelength clear-air eddies and 750-km-wavelength mesocyclones associated with a synoptic-scale midlatitude cyclone. *Mon. Wea. Rev.*, **124**, 1199–1210.
- Monaldo, F. M., 2000: The Alaska SAR demonstration and near-real-time synthetic aperture radar winds. *Johns Hopkins APL Tech. Dig.*, **21**, 75–79.
- , D. R. Thompson, R. C. Beal, W. G. Pichel, and P. Clemente-Colón, 2001: Comparison of SAR-derived wind speed with model predictions and ocean buoy measurements. *IEEE Trans. Geosci. Remote Sens.*, **39**, 2587–2600.
- , —, W. G. Pichel, and P. Clemente-Colón, 2004: A systematic comparison of QuikSCAT and SAR ocean surface wind speeds. *IEEE Trans. Geosci. Remote Sens.*, **42**, 283–291.
- Mourad, P. D., 1999: Footprints of atmospheric phenomena in synthetic aperture radar images of the ocean surface—A review. *Air–Sea Exchange: Physics, Chemistry, and Dynamics*, G. L. Geernaert, Ed., Kluwer Academic, 269–290.
- Neiman, P. J., and M. A. Shapiro, 1993: The life cycle of an extratropical marine cyclone. Part I: Frontal-cyclone evolution and thermodynamic air–sea interaction. *Mon. Wea. Rev.*, **121**, 2153–2176.
- , —, E. G. Donall, and C. W. Kreitzberg, 1990: Diabatic modification of an extratropical marine cyclone warm sector by cold underlying water. *Mon. Wea. Rev.*, **118**, 1576–1590.
- , —, and L. S. Fedor, 1993: The life cycle of an extratropical marine cyclone. Part II: Mesoscale structure and diagnostics. *Mon. Wea. Rev.*, **121**, 2177–2199.
- Orlanski, I., 1975: A rational subdivision of scales for atmospheric processes. *Bull. Amer. Meteor. Soc.*, **56**, 527–530.
- Parsons, D. B., and P. V. Hobbs, 1983: The mesoscale and microscale structure and organization of clouds and precipitation in midlatitude cyclones. XI: Comparisons between observational and theoretical aspects of rainbands. *J. Atmos. Sci.*, **40**, 2377–2398.
- Physick, W. L., 1988: Mesoscale modeling of a cold front and its interaction with a diurnally heated land mass. *J. Atmos. Sci.*, **45**, 3169–3187.
- Rosmond, T. E., 1981: Navy Operational Global Atmospheric Prediction System. Preprints *Fifth Conf. on Numerical Weather Prediction*, Monterey, CA, Amer. Meteor. Soc., 74–79.
- Schultz, D. M., D. Keyser, and L. F. Bosart, 1998: The effect of large-scale flow on low-level frontal structure and evolution in midlatitude cyclones. *Mon. Wea. Rev.*, **126**, 1767–1791.
- Sikora, T. D., G. S. Young, R. C. Beal, and J. B. Edson, 1995: Use of spaceborne synthetic aperture radar imagery of the sea surface in detecting the presence and structure of the convective marine atmospheric boundary layer. *Mon. Wea. Rev.*, **123**, 3623–3632.
- , —, H. N. Shirer, and R. D. Chapman, 1997: Estimating convective atmospheric boundary layer depth from microwave radar imagery of the sea surface. *J. Appl. Meteor.*, **36**, 833–845.
- , —, R. C. Beal, F. M. Monaldo, and P. W. Vachon, 2005: Applications of synthetic aperture radar in marine meteorology. *Advances in Fluid Mechanics: Atmosphere Ocean Surface Interactions*, Vol. 2, W. Perrie, Ed., Wessex Institute of Technology, in press.
- Simpson, J. E., 1972: Effects of the lower boundary on the head of a gravity current. *J. Fluid Mech.*, **53**, 759–768.
- Vachon, P. W., J. A. Johannessen, and D. P. Browne, 1995: *ERS-1* SAR images of atmospheric gravity waves. *IEEE Trans. Geosci. Remote Sens.*, **33**, 1014–1025.
- Weissman, D. E., M. A. Bourassa, and J. Tongue, 2002: Effects of

- rain rate and wind magnitude on SeaWinds scatterometer wind speed errors. *J. Atmos. Oceanic Technol.*, **19**, 738–746.
- Winstead, N. S., T. D. Sikora, D. R. Thompson, and P. D. Mourad, 2002: Direct influence of gravity waves on surface-layer stress during a cold air outbreak, as shown by synthetic aperture radar. *Mon. Wea. Rev.*, **130**, 2764–2776.
- Young, G. S., and R. H. Johnson, 1984: Meso- and microscale features of a Colorado cold front. *J. Climate Appl. Meteor.*, **23**, 1315–1325.
- , and T. D. Sikora, 2003: Mesoscale stratocumulus bands caused by Gulf Stream meanders. *Mon. Wea. Rev.*, **131**, 2177–2191.
- , S. M. Perugini, and C. W. Fairall, 1995: Convective wakes in the equatorial western Pacific during TOGA. *Mon. Wea. Rev.*, **123**, 110–123.
- , J. A. Harlan, and T. M. Georges, 1997: Application of over-the-horizon radar observations to synoptic and mesoanalysis over the Atlantic. *Wea. Forecasting*, **12**, 44–55.